Accurate estimate of drag forces using particle-resolved direct numerical simulations

Mohamed-Amine Chadil, Stéphane Vincent, Jean-Luc Estivalèzes

Accurate estimate of drag forces using particle-resolved direct numerical simulations

Mohamed-Amine Chadil · Stéphane Vincent · Jean-Luc Estivalèzes ·

Received: date / Accepted: date

Abstract An accurate force estimate for finite-size particle simulations is proposed based on Lagrange extrapolation of third order, coupled with a Taylor interpolation of same order, to estimate pressure and viscous constraints on the surface of particles. The main point of our approach is to upwind the interpolation support in the normal direction to the fluid/solid interface so as to use only fluid values to estimate forces. Also, detailed validations of forces are considered for estimating accuracy and convergence order of the method on various incompressible motions such as the flow around an isolated particle at various Reynolds numbers and flows across packed spheres under Faced-Centered Cubic, random and bi-disperse arrangements.

Keywords Accurate drag force calculation · Finite size particles · Immersed boundary techniques · Penalty methods · Fixed arrangements of spheres

1 Introduction

In the framework of finite-size particle motions, the numerical simulation of a particulate flow interacting with a surrounding fluid can be investigated

M.-A. Chadil
Institut de Mécanique des Fluides de Toulouse, IMFT, Université de Toulouse, CNRS - Toulouse, France
Institut de Mécanique et Ingénierie (I2M), Université de Bordeaux, France
E-mail: achadil@imft.fr

S. Vincent
Laboratoire MSME, UMR CNRS 8208, Université Paris-Est Marne-La-Vallée, France
stephane.vincent@u-pem.fr

J.-L. Estivalèzes
The French Aerospace Lab, ONERA, Toulouse, France
Institut de Mécanique des Fluides de Toulouse, IMFT, Université de Toulouse, CNRS - Toulouse, France
jean-luc.estivalezes@onera.fr

following two different numerical strategies: unstructured or structured grids. This important choice is in particular motivated by the instantaneous description of the evolving complex shape represented by the interface between the carrier fluid and a set of moving particles. On the one hand, the more natural discretization seems to be the implementation of an unstructured body-fitted grid to simulate the fluid area in the two-phase particle flow [1] [2] [3] [4]. Building such a finite-volume or finite-element mesh in three-dimensions is not easy and requires automatic remeshing as the solid particles move according to time and space. The remeshing process at each calculation step is time consuming and can be very difficult to manage automatically in computer softwares when the global shape of the fluid-solid interface is changing at each calculation step [5]. On the other hand, it can be imagined to develop a fixed structured grid approach to simulate particulate flows. With this method, the mesh is not adapted to the fluid-solid interfaces and includes both phases. On a mesh point of view, this approach is simpler than the previous one. The difficulty lies in taking into account the presence of particles in the fluid whose interface is not explicitly tracked by the mesh that does not conform to the fluid/particle interface. This type of modeling and numerical problem belongs to the class of fictitious domains [6] [7]. The penalty modeling strategy[8] [9] [10] developed hereafter is based on this approach and will be reported in the next section.

One major interest of finite-size particle motion simulation is to provide a local estimate of all flow characteristics (velocity, pressure, viscous stress) together with a local description of the particle-fluid interface. The resolved scale particle motion does not require any force modeling nor interaction model as soon as the mesh is refined enough. In the present work, we will demonstrate that having at least 5 points in the boundary layer attached to a given particle allows to recover all the physics of the particle flow without using any force or interaction model (drag, lift, lubrication, etc). As a consequence, the finite-size particle approach can be considered as a kind of fully resolved Direct Numerical Simulation (DNS) of the particulate flow as soon as no modeling is required to solve the problem. The mesoscopic or macrocopic particle flow models (Eulerian-Lagrangian, Eulerian-Eulerian) do require the knowledge of interaction forces to close specific particle-motion interaction terms. For an isolated particle in an infinite medium, the drag force law of Schiller and Naumann [11] is well known and often used in large scale models. For fixed and moving beds of particles, we can cite the correlations based on experiments proposed by Ergun [12] and Wen&Yu [13] and also Gobin [14] who proposed a correlation based on these two correlations. As soon as the solid fraction is high and the particle size or shape of particles is not constant (bi-dispersed flows, spheroidal particles, etc), drag and lift laws have to be designed. This is the main objective of the present work, *i.e.* providing a DNS framework with accurate force calculation in order to finally obtain new force laws for various particulate motions.

Numerous numerical works have been devoted to performing DNS of finite-size particulate flows and obtaining resulting drag force laws from the macroscopic analysis of local flow motions in the vicinity of the particle surface. The first class of numerical models, generally investigated for fixed arrangements of particles, is the Lattice Boltzmann approach. It was used in numerous works by Ladd [15] [16] for particle suspensions, by Hill *et al.* [17] for monodiperse face cubic centered (FCC) array of spheres, by Hoef *et al.* [18] and beetstra *et al.* [19] for random monodisperse and bidisperse array of spheres to cite a few. Another class of very popular methods for handling finite-size particle is the Immersed Boundary Method (IBM) coupled with incompressible Navier-Stokes equations initially developped for particulate flows by [20] [21]. For random monodisperse array of spheres, the work of Tenneti *et al.* [22] is very interesting as it covers a wide range of solid fractions $\alpha_d = 0.1 - 0.4$, and also Reynolds number up to 300. At the end, a new correlation is proposed for drag force laws. The last interesting class of numerical approaches is the body fitted mesh method, that is restricted to fixed array of particles as it is impossible to generate automatically a three-dimensional mesh that adapts to the motion of particles. Among the most interesting works in the field, we can cite the simulations and analysis of Massol *et al.* [23] for monodispersed FCC arrays of spheres.

In all these numerical approaches, the drag force can be deduced in different ways:

- with Darcy penalty methods [24], it can be obtained directly from the source term used to accelerate the fluid ouside the particles.
- with the LBM, the drag force exerted by the fluid on the particles is calculated according to the momentum exchange algorithm of Ladd [15].
- In the IBM approach, the forces exerted by the fluid on the particles can be deduced from the reaction IBM force imposed in the momentum equations to satisfy a solid behaviour [25].
- with the Volume Penalty Method (VPM), Bizid [26] uses Taylor extrapolations to get the pressure and viscous stress projection on particle surface.

In the framework of macroscopic Eulerian-Eulerian or mesoscopic Eulerian-Lagrangian models, the previously cited drag force laws are used in many industrial processes such as fluid catalytic cracking reactors [27], gas phase polymerisation reactors [14], chemical looping [28] or fluidized beds [10] [29]. However, convergence studies and accuracy analysis of force calculation have rarely been considered.

Our major contribution is to propose an accurate force estimate for finite-size particle simulations. Even if all full DNS of particle flows extract forces on particles [10] [20] [30] [2], few works report on how practically these forces can be calculated and what is the accuracy or convergence order of the forces. Among the wide literature devoted to full DNS of particle motions, we can cite the work of Bizid [26] [31] who uses Taylor extrapolation to estimate pressure

and viscous constraints on the particle surface. This approach is of low accuracy as it utilizes velocity and pressure values that can be inside the particle volume. The most advanced work on force calculation on immersed interfaces is due to Zastawny *et al.* [32] with an improved mirroring immersed boundary method. In the present work, a new force calculation is proposed based on Lagrange extrapolation of third order, coupled with a Taylor interpolation of same order. The main point of our approach is to upwind the interpolation support in the normal direction to the fluid/solid interface so as to use only fluid values to estimate forces. Detailed validations of forces are considered for estimating accuracy and convergence order of the proposed method.

The article is structured as follows. A presentation of the models and numerical methods is first proposed in section 2, paying attention to describe fictitious domain and penalty methods used to model and approximate incompressible particulate motions. In the third section, a new force calculation for immersed interfaces is proposed, with discussions conducted on order of approximations and associated accuracy. Validations for flows interacting with isolated spherical particles at various Reynolds number are presented in the fourth section. Section 5 is devoted to simulations and validations of flows through fixed arrangements of mono- and bi-dispersed spheres. Finally, conclusions and perspectives are drawn.

2 Model and numerical methods

2.1 Fictitious domain approach

The modeling and simulation of moving objects (bubbles, droplets, solid particles) interacting with a carrier fluid is impossible to realize with unstructured meshes as soon as these objects deform or move in a 3D geometry. The commonly developed alternative approach consists in simulating this kind of flow on a fixed grid and to locate the interface thanks to an auxiliary phase function such as Volume Of Fluid or Level Set functions [33]. The concept that disconnects the interface motion and the mesh used to solve the conservation equations is called fictitious domain approach [7] [34]. Indeed, from the motion equation point of view, the interface is not known, only its presence is taken into account thanks to a volume auxiliary function. In these approaches, the interface tracking and the associated building of the phase function is of primary importance.

As proposed in [10], incompressible two-phase flows involving a carrier fluid and a solid phase can be modeled on a fixed mesh with fictitious domain approaches by considering the incompressible Navier-Stokes equations together with a phase function C describing the particle phase shape evolutions through an advection equation on the corresponding phase function. As explained by Kataoka [35] for fluid/fluid two-phase flows and Vincent [10] for particle flows,

the resulting model takes implicitly into account the coupling between different phases separated by resolved interfaces, *i.e.* larger than the mesh cell size. The motion equations reads

$$\nabla \cdot \mathbf{u} = 0 \quad (1)$$

$$\rho \left(\frac{\partial \mathbf{u}}{\partial t} + (\mathbf{u} \cdot \nabla)\, \mathbf{u} \right) = -\nabla p + \rho \mathbf{g} + \nabla \cdot \left[\mu (\nabla \mathbf{u} + \nabla^t \mathbf{u}) \right] + \mathbf{F}_{si} + \mathbf{F}_m \quad (2)$$

$$\frac{\partial C}{\partial t} + \mathbf{u} \cdot \nabla C = 0 \quad (3)$$

where $\mathbf{u}$ is the velocity, p the pressure, t the time, $\mathbf{g}$ the gravity vector, ρ and μ respectively the density and the viscosity of the equivalent fluid. The two-way coupling between particle and fluid motions is ensured in the momentum equations by the presence of a solid interaction force $\mathbf{F}_{si}$ [36] [37] which is not considered in the present work as only fixed particles are dealt with. The source term $\mathbf{F}_m$ is used to impose a flow rate to the fluid.

The one-fluid model is almost identical to the classical incompressible Navier-Stokes equations, except that

- the local properties of the equivalent fluid (ρ and μ) depend on C. In the present work, an arithmetic average is used for density and an harmonic average is considered for viscosity [10].
- the interface localization requires the solving of an additional equation on C. Instead of solving this equation on the Eulerian mesh, which is source of numerical diffusion or tearing of interfaces, a Lagrangian representation is preferred. A specific mesh (linear elements in 2D and set of triangles in 3D) is considered for the particle surface S. Equation (3) is reformulated as $\frac{d\mathbf{X}_b}{dt} = \mathbf{V}_p$, with $\mathbf{X}_b$ the centroid of the spherical particle and $\mathbf{V}_p$ the velocity of the particle interpolated with surrounding Eulerian velocities coming from the solving of equations (1-2). The approximation of the Lagrangian tracking of $\mathbf{X}_b$ is detailed in [10]. Once $\mathbf{X}_b$ is known, the position of each particle surface mesh element is also known. The phase function C is automatically build by projecting the Lagrangian particle mesh onto the Eulerian mesh [33]. For non-spherical particles the rotational motion has to be considered. It is for example solved with Quaternions [38]. In the present work, only fixed arrangements of particles are dealt with. As a consequence, the Lagrangian particle tracking is not considered even if the Lagrangian mesh for representing particles is used to calculate forces.

Satisfying the incompressible and solid constraints in fluid and particles requires developing a specific model. Two penalty approaches are proposed and detailed in the next section to tackle with these constraints.

2.2 Penalty methods

As explained in the previous section, the one-fluid model and the fictitious domain approach formulated for dealing with particle flows require to consider each different phase (fluid, solid) as a fluid domain with specific material properties (density and viscosity for an isothermal flow). Each sub-domain is located by a phase function C.

In addition to local physical characteristics of the fluid that change over time due to particle motion, the local constraints that have to be fulfilled change potentially at each time step. Indeed, a given point or cell can be inside a fluid zone at time $n\Delta t$ and can be solid at the next time step $(n+1)\Delta t$. Here, n is the time index and Δt the associated time step. Two different numerical methods are used to satisfy in a coupled way and at the same time the fluid incompressibility and the solid behavior:

- Ensuring the solid behavior in the solid zones where $C = 1$ requires to define a specific rheological law for the rigid fluid part without imposing the velocity, as the particle velocities are not always known *a priori* in particulate motions (particle sedimentation, fluidized beds, turbulence particle interaction). A specific model is implemented for handling the solid particle behavior in the one-fluid Navier-Stokes equations. It is based on a decomposition of the viscous stress tensor and on a penalty method that acts on the viscosity which tends to large values in the particles [39] to implicitly impose the solid behavior and also the coupling between fluid and solid motion. For fixed particles, the velocity of the cell containing the centroid of the particle is imposed equal to zero. The viscous penalty method propagates the zero velocity in the whole solid medium.
- Following a similar walkthrough as in the work on Stokes and Navier-Stokes equations proposed by Fortin and Glowinski [40], an augmented Lagrangian method is applied to the unsteady Navier-Stokes equations dedicated to particulate flows. The main objective is to deal with the coupling between velocity and pressure and to satisfy the fluid and solid constraints at the same time. Starting with $\mathbf{u}^{*,0} = \mathbf{u}^n$ and $p^{*,0} = p^n$, the augmented Lagrangian solution reads
  while $||\nabla \cdot \mathbf{u}^{*,\mathbf{m}}|| > \epsilon$, solve

$$\begin{gathered}(\mathbf{u}^{*,0}, p^{*,0}) = (\mathbf{u}^n, p^n) \\ \rho\left(\frac{\mathbf{u}^{*,m} - \mathbf{u}^{*,0}}{\Delta t} + \mathbf{u}^{*,m-1} \cdot \nabla \mathbf{u}^{*,m}\right) - \nabla(r\nabla \cdot \mathbf{u}^{*,m}) \\ = -\nabla p^{*,m-1} + \rho\mathbf{g} + \nabla \cdot [\mu(\nabla \mathbf{u}^{*,m} + \nabla^T \mathbf{u}^{*,m})] + \mathbf{F}_{si} + \mathbf{F}_m \\ p^{*,m} = p^{*,m-1} - r\nabla \cdot \mathbf{u}^{*,m}\end{gathered} \tag{4}$$

  where r is an augmented Lagrangian parameter used to impose the incompressibility constraint, m is an iterative convergence index and ϵ a numerical threshold controlling the constraint. The augmented Lagrangian

method is a kind of penalty technique: if $r \to +\infty$, the incompressibility is imposed but the solving of the linear system is difficult with iterative solvers while $r \to 0$ does not act on the fluid constraint and keeps the conditioning of the matrix unchanged. Usually, a constant value of r is used, for example equal to the average between the minimum and maximum eigenvalues of the linear system for Stokes flows [40]. From numerical experiments, optimal values are found to be of the order of ρ_i and μ_i in each phase (fluid or solid) to accurately solve the motion equations in the related zone [8] [9]. Algebraic improvements have also been proposed by Vincent [41] to automatically estimate the local values of r. In the present work, a constant value of r will be used. Its magnitude will be discussed in the validation sections.

2.3 Discretization schemes and solvers

The schemes and solvers used in the present work are detailed in [10]. The mass and momentum conservation equations, containing the viscous and augmented Lagrangian penalty terms, are discretized with implicit finite volumes on structured staggered meshes. The time derivative is approximated with a first or second order Euler scheme while the inertial, viscous and augmented Lagrangian terms are discretized with a second-order centered scheme. All fluxes are written at time $(n+1)\Delta t$, except the non-linear inertial term that is linearized at first or second order as follows

- $\mathbf{u} \cdot \nabla \mathbf{u} \approx \mathbf{u}^n \cdot \nabla \mathbf{u}^{n+1}$ for first order linearization
- $\mathbf{u} \cdot \nabla \mathbf{u} \approx \left(2\mathbf{u}^n - \mathbf{u}^{n-1}\right) \cdot \nabla \mathbf{u}^{n+1}$ for second order Adams-Bashforth like linearization

The obtained linear system is solved with a BiCGSTAB II iterative solver [42], preconditionned with a Modified and Incomplete LU approach [43]. All the code is working on massively parallel computers by using MPI devices and exchanges [10].

3 Lagrangian extrapolation of forces for immersed boundary methods

The drag force due to the fluid-solid interaction at a surface S of the solid phase is:

$$\mathbf{F}^D = \mathbf{F}_p + \mathbf{F}_v \tag{5}$$

where the pressure force $\mathbf{F}_p$ and the viscous force $\mathbf{F}_v$ are:

$$\mathbf{F}_p = \oint_S -p\,\mathbf{n}\;\; dS \tag{6}$$

$$\mathbf{F}_v = \oint_S 2\mu\overline{\overline{\sigma}}.\mathbf{n}\;\; dS \tag{7}$$

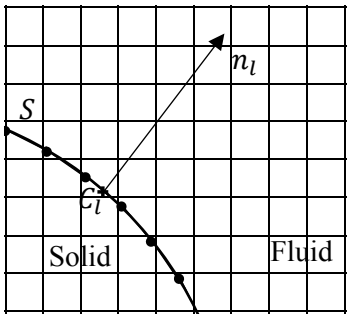

Fig. 1: Details of a 2D discretization of the particle surface S used in drag force computation

Here, $\overline{\overline{\sigma}}$ is the fluid viscous stress tensor.

The computation of these forces consists in discretizing S on a set of N elements (triangles in $3d$ and segments in $2d$) called Lagrangian mesh (see figure 1), such that:

$$\mathbf{F}_p \approx \sum_{l}^{N} -p_l \ \mathbf{n}_l \ \ dS_l \tag{8}$$

$$\mathbf{F}_v \approx \sum_{l}^{N} 2\mu\overline{\overline{\sigma}}_l.\mathbf{n}_l \ \ dS_l \tag{9}$$

where p_l, $\overline{\overline{\sigma}}_l$ and $\mathbf{n}_l$ are respectively the pressure, strain tensor and outgoing normal vector at the center $\mathbf{C}_l$ of the l^{th} element of the Lagrangian mesh as illustrated in figure 1. Normal $\mathbf{n}_l$ and element surface dS_l are deduced from the coordinates of the nodes constituting the l^{th} element.

3.1 Low order naive approach

Given that the pressure field p and the viscous stress tensor $\overline{\overline{\sigma}}$, used in the drag force computation, are known on the Eulerian mesh and not on the Lagrangian mesh as explained above, the naive approach to overcome this problem consist in interpolating them from the Eulerian mesh on the Lagrangian mesh using a second order Taylor interpolation detailed in Appendix 1.

To validate this approach, we compute the drag force exerted by a uniform Stokes flow ($Re = 10^{-3}$) on an isolated cylinder (2D) and an isolated sphere (3D), as detailed below.

Uniform Stokes flow past a cylinder

According to [31], a uniform Stokes flow past a cylinder of diameter $d = 2m$, with the undisturbed velocity being noted $U_\infty = 1m/s$, is solution of the Brinkman equation $-\nabla p + \mu \Delta \mathbf{u}_i - \dfrac{\mu}{K}\mathbf{u}_i = 0$. In the polar coordinate frame (r, θ) centered on the particle, it reads:

$$\mathbf{u}\left(r,\theta\right) = \begin{cases} \frac{1}{r}\left(-\left(1+\frac{2K_1(\lambda)}{\lambda K_0(\lambda)}\right)\frac{1}{r} + r + \frac{2}{\lambda K_0(\lambda)}K_1(\lambda r)\right)\cos\theta \\ -\left(1+\left(1+\frac{2K_1(\lambda)}{\lambda K_0(\lambda)}\right)\frac{1}{r^2} - \frac{2}{K_0(\lambda)}\left(K_0(\lambda r) + \frac{K_1(\lambda r)}{\lambda r}\right)\right)\sin\theta \end{cases} \tag{10}$$

$$p\left(r,\theta\right) = \mu\lambda^2\left(-\left(1+\frac{2K_1(\lambda)}{\lambda K_0(\lambda)}\right)\frac{1}{r} - r\right)\cos\theta \tag{11}$$

The corresponding drag force is:

$$\mathbf{F}^D = \frac{2\pi}{Re}\left(2\lambda^2 + 4\frac{\lambda K_1(\lambda)}{K_0(\lambda)}\right)\mathbf{e}_x \tag{12}$$

where $\lambda = \dfrac{d^2}{4K}$ is the dimensionless permeability of the porous medium in Brinkman sens, K is the permeability of the porous cylinder, K_0 and K_1 are the modified Bessel functions of rank 0 and 1. For $K \to 0$, the porous cylinder can be likened to an impermeable solid particle.

Uniform Stokes flow past a sphere

For the uniform flow past a sphere in Stokes regime, the velocity and pressure are [44] :

$$\mathbf{u}\left(x,y,z\right) = \begin{cases} U_\infty - \frac{3}{4}(\frac{d}{2})U_\infty\left(\frac{x^2}{r^3} + \frac{1}{r}\right) + \frac{3}{4}(\frac{d}{2})^3 U_\infty\left(\frac{x^2}{r^5} - \frac{1}{3r^3}\right) \\ \frac{3}{4}U_\infty\left(\frac{(\frac{d}{2})^3}{r^5} - \frac{(\frac{d}{2})}{r^3}\right)xy \\ \frac{3}{4}U_\infty\left(\frac{(\frac{d}{2})^3}{r^5} - \frac{(\frac{d}{2})}{r^3}\right)xz \end{cases} \tag{13}$$

$$p = -\frac{3}{4}\mu d U_\infty \frac{x}{r^3} \tag{14}$$

where $r = \sqrt{x^2 + y^2 + z^2}$.

The drag force is analytically given by:

$$\mathbf{F}^D = 3\pi\mu d U_\infty \mathbf{e}_x \tag{15}$$

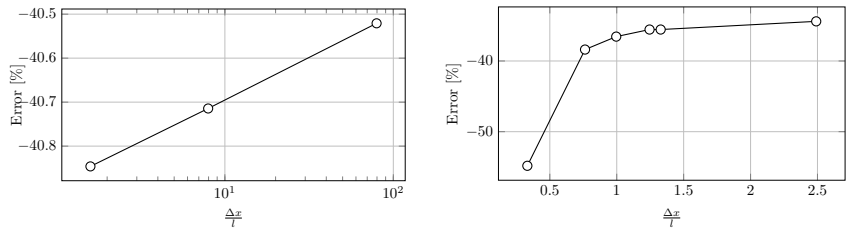

Fig. 2: Drag force relative error (%) for the Stokes flow past a cylinder (left), and the Stokes flow past a sphere (right) in terms of Lagrangian mesh refinement - the force is computed with the naive 2^{nd} order Taylor interpolation method. The size of the Lagrangian particle surface mesh element is l while the size of the Cartesian Navier-Stokes mesh is Δx.

Simulations setup

The computational domain used to simulate a uniform Stokes flow past a cylinder (resp. a sphere) is a square (resp. a cube) of a Length $L = 2d$, and the spatial discretization, using a regular Cartesian grid called Eulerian mesh, is represented by the number of grid cells across the diameter of the particle $D_m = \dfrac{d}{\Delta x} = 20$. The exact solution (10), (11) (resp. (13), (14)) for a Stokes flow past a cylinder (resp. a sphere) was implemented at boundary conditions to be able to simulate such a flow in a numerically small domain not extending to infinity as Stokes flow would require. Practically, the considered simulation domain is two particle diameter long in each space direction.

Results

Figure 2 shows that the computation of the drag force with a naive approach is not accurate, the error being about at least 40% even if the surface Lagrangian mesh is refined. This is due to the use of pressure and strain tensor values in the cells containing the fluid-solid interface where the error with the analytic solution is the highest, as illustrated in figure 3 for the uniform flow past a cylinder ($2D$) and a sphere ($3D$). This error is due to the fact that the physical characteristics (μ, ρ) in the mixed fluid-solid cells are the average between those of the fluid and those of the solid.

To prevent the use of wrong pressure and velocities in the cells cut by the fluid-particle interface, we have to extrapolate the pressure and the strain tensor from the fluid area far from the particle to the interface. To do so, a Lagrange extrapolation is considered, as detailed below.

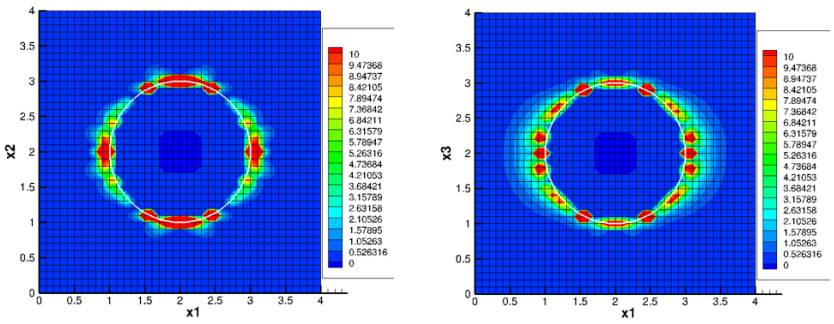

Fig. 3: Relative error (%) of the first component of velocity for Stokes flow past cylinder (left) and Stokes flow past sphere (right) in the whole domain

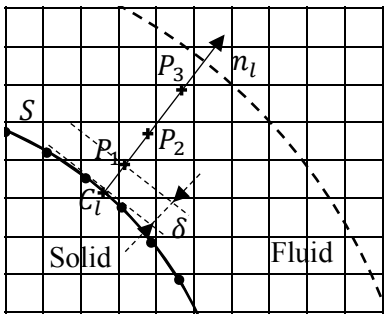

Fig. 4: Details of third order Lagrange extrapolation used in drag force computation

3.2 New high order method based on Lagrange extrapolation

Given a function $f : X \in \mathbb{R}^3 \to \mathbb{R}$ and a set of k points $\mathbf{P}_i, i = 1..k$, the k^{th} Lagrange extrapolation of f at point $\mathbf{C}_l$ is given by:

$$f(\mathbf{C}_l) = \sum_{i=1}^{k} f(\mathbf{P}_i) L_i(\mathbf{C}_l) \quad , where \qquad L_i(\mathbf{C}_l) = \sum_{j \neq i}^{k} \frac{|\mathbf{C}_l - \mathbf{P}_j|}{|\mathbf{P}_i - \mathbf{P}_j|} \tag{16}$$

The k^{th} order of the drag force computation consists now of interpolating (using the k^{th} order Taylor interpolation detailed in Appendix 1) the pressure and the strain tensor on k $\mathbf{P}_i$ fictitious points built along the normal (see figure 4 for third order), and then using the k^{th} order Lagrange extrapolation (16) to compute them at $\mathbf{C}_l$. With (5), (8), (9), the friction force exerted by the fluid on the particle can be calculated.

In figure 4, points P_1, P_2 and P_3 are the fictitious points used in third order Lagrange extrapolation of the pressure and viscous components of the

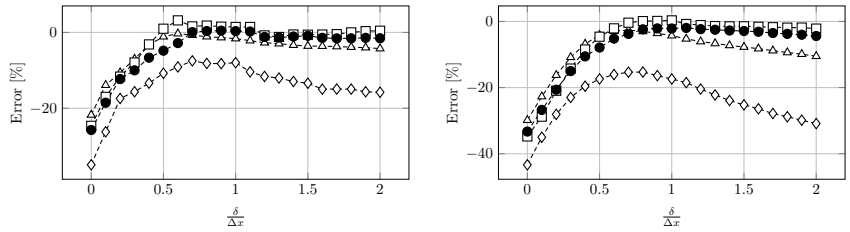

Fig. 5: Drag force relative error (%) according to extrapotation distance δ (written in Δx unit) for the Stokes flow past a cylinder (left) and the Stokes flow past a sphere (right) at different order: (◇) first, (△) second, (●) third, and (□) fourth orders are plotted.

force on the particle surface. The zone between the particle surface S (solid line) and the dash line corresponds to the Eulerian discrete points that have an influence on the force calculation. Parameter δ is the minimum distance between the first fluid point and S that is required to obtain a correct force estimate.

Note that the order of the drag force computation may not be the same on all the Lagrangian mesh element. Indeed the choice of the computation order located at the centre $\mathbf{C}_l$ of each Lagrangian mesh element is governed by the fact that all the points used in the Lagrange extrapolation and the Taylor interpolation have to be fully fluid, *i.e* the fluid-phase indicator function $C = 0$ on these points.

Considering that the pressure and strain tensor have to be extrapolated from the nearest fluid region in the vicinity of the particle, where the physical characteristics belong to the fluid, to the interface region where the drag force is computed, the first step consists in increasing the distance δ (see figure 4) until the computation of the force is accurate enough. As illustrated in figure 5, the minimum error is reached for $\delta = \Delta x$ and remains stable for the third and fourth order Lagrange interpolation, for both simulations, namely the Stokes flow past a cylinder (left), and past a sphere (right) . As a consequence, the third order force computation with $\delta = \Delta x$ will be considered thereafter as it requires less computational effort. The errors obtained with the new high order force calculation method are reported in figure 6. Compared to the naive approach, the error levels for both cylinder and sphere cases are now always less or around 2% as soon as the local size of the Lagrangian surface mesh elements is comparable to Δx. Thanks to the novel force estimate, the error has been reduced by a factor of 20. In the rest of the work, the value of δ will be chosen to be Δx if not specified.

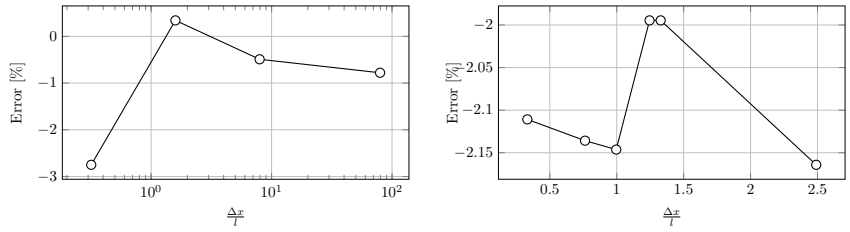

Fig. 6: Drag force relative error (%) for the Stokes flow past a cylinder (left) and the Stokes flow past a sphere (right) in term of the Lagrangian mesh refinement l: force computed using 3^{rd} Lagrange extrapolation and 2^{nd} order Taylor interpolation

4 Validation on flows interacting with an isolated particle

4.1 Drag coefficient

For validation purpose, the force acting on a particle and in particular the corresponding drag coefficient is recalled. It is defined as [45]:

$$C_d = \frac{|\mathbf{F}^D|}{\frac{1}{2}\rho \tilde{U}^2 A_p} \tag{17}$$

where $\tilde{U} = |U_\infty \mathbf{e}_x - \mathbf{U}_p|$ is the relative velocity between the particle and the fluid velocity at infinity, $U_\infty \mathbf{e}_x$ is fluid velocity in the mean flow direction far from the particle, $\mathbf{U}_p$ is the particle velocity, ν is the fluid kinematic viscosity and $A_p = \frac{\pi}{4} d^2$ the cross-sectional area of the particle.

The drag coefficient is dependent on the flow regime determined by the Reynolds number:

$$Re = \frac{\tilde{U} d}{\nu} \tag{18}$$

The drag coefficient in Stokes regime, *i.e.* when $Re \to 0$, is:

$$C_d = \frac{24}{Re} \tag{19}$$

The correlation of drag coefficient for a finite Reynolds number, proposed by Schiller & Naumann [11] is:

$$C_d = \frac{24}{Re}\left(1 + 0.15\ Re^{0.687}\right) \tag{20}$$

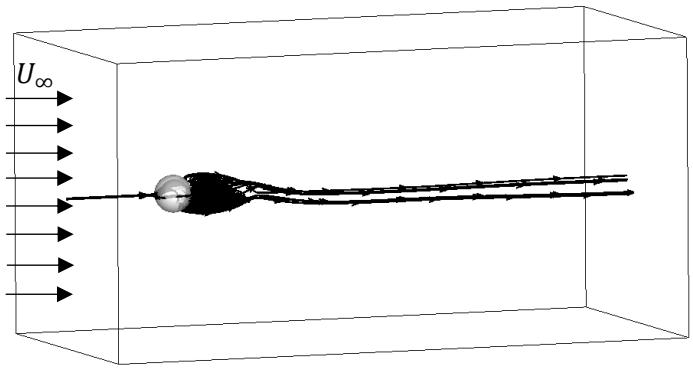

Fig. 7: Illustration of instantaneous stream lines obtained for a uniform flow past an isolated sphere at Re=290. The upstream unperturbed velocity U_∞ is imposed at the left boundary condition.

4.2 Simulations setup

The computational domain is first chosen, its lengths being $L_x = 16d$ and $L_y = L_z = 8d$ in each Cartesian direction. The Eulerian mesh refinement is constant in a box of extension $[(2d, 3d, 3d)\,; (6d, 5d, 5d)]$ centered around the particle position. Outside this box, the Eulerian mesh is exponentially coarsen from the box to the boundaries of the simulation domain. Accurate drag force calculation needs properly resolved boundary layers around the particle. It is expected that a 5 cell resolution in the boundary layer thickness will be enough at least for the range of Reynolds numbers studied in the present article. This choice is also consistent with the compact support of cells needed to get third order Lagrange extrapolation accuracy (see figure 24 in appendix 1). This gives $\dfrac{d}{\sqrt{Re}} = 5\Delta x$ according to scaling laws for laminar dynamic boundary layers. Therefore, in the box surrounding the particle, the minimum cell size is:

$$\Delta x = \frac{d}{5\sqrt{Re}} \tag{21}$$

The inlet boundary conditions is $\mathbf{u} = U_\infty \mathbf{e}_x$ (see figure 7) and Neumann conditions are applied elsewhere.

4.3 Study of numerical parameters for the Lagrange extrapolation

As an extension of the work carried out for the Stokes regime, we have performed the same kind of study for a higher finite Reynolds number $Re = 100$ when inertial effects are important. The effect on the drag force computation

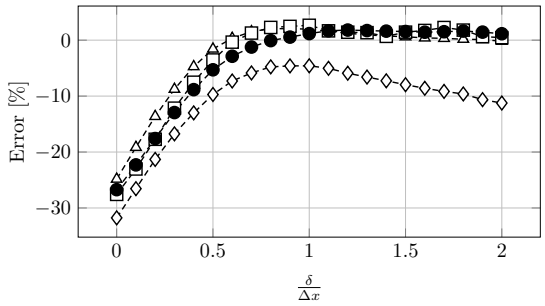

Fig. 8: Drag force relative error (%) for the uniform flow past sphere at $Re = 100$. Different orders of Lagrange extrapolation are considered: (◇) first, (△) second, (●) third, and (□) fourth order. The distance between the first Eulerian point used to extrapolate forces and the particle surface is δ.

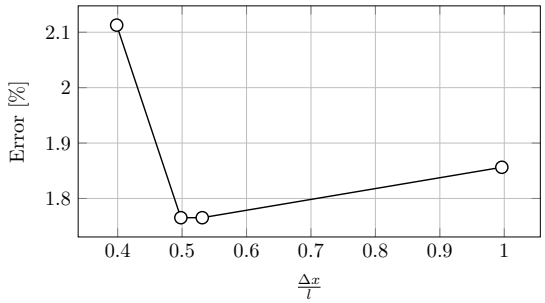

Fig. 9: Drag force relative error (%) according to Lagrangian surface element size l for uniform flow past sphere at $Re = 100$.

of the distance δ between the particle interface points $\mathbf{C}_l$ and the first Eulerian mesh extrapolation point P_1 has been considered. The role played by the Lagrangian mesh refinement have also been analyzed.

One can observe in figure 8 a similar behaviour of error as already found for Stokes flows (the reader can refer to figure 5 right) indicating that in this range, Reynolds number have little influence on drag force errors at least for 2^{nd}, 3^{rd} and 4^{th} order Lagrange extrapolations. To conclude on the distance between Eulerian interpolation points and particle surface, as soon as $\delta \geq \Delta x$, the error on drag force calculation is less than 2% for 3^{rd} and 4^{th} order Lagrange extrapolation in Stokes and Navier-Stokes regimes. In this case, a 3^{rd} order Lagrange extrapolation is considered, as being a good compromise between implementation complexity, calculation time and accuracy.

As illustrated in figure 9, the Lagrangian mesh refinement does not affect a lot the drag force computation as soon as the Lagrangian particle surface element size l is of the order of Δx. For $Re = 100$, the error is around 2% on

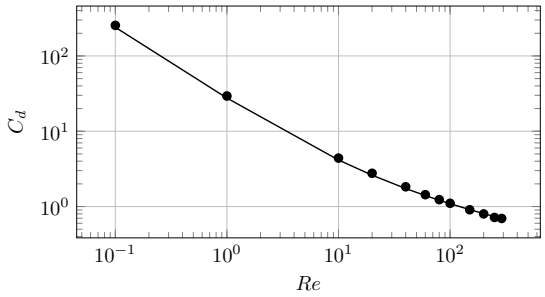

Fig. 10: Drag coefficient for uniform flow past sphere at different Reynolds number: (——) Schiller & Naumann [11], (●) present work.

the drag force calculation.

In the rest of the present work, the 3^{rd} order Lagrange extrapolation will always be used together with $l = \Delta x$.

4.4 Result on the drag coefficient

The transition area between axisymmetric flow and non-axisymmetric vortex shedding regime being around $Re = 300$, for a uniform flow past a fixed isolated sphere, we have conducted several simulations for Reynolds numbers up to 290 ($Re = 0.1, 1, 10, 20, 40, 60, 80, 100, 150, 200, 250, 290$). In each case, the simulations are stopped when the steady state of the flow is reached. The drag coefficient obtained at the final step of each simulation is compared to the correlations (19) and (20). Figure 10 shows a very good agreement of the numerically calculated drag coefficient compared to the correlation of Schiller & Naumann [11]. This test case provides an interesting validation of the force calculation for a single particle.

4.5 Pressure coefficient

The analysis of local pressure profiles can give insight into the pressure behavior depending on the Reynolds number. The local pressure coefficients are defined by equation (22) in a spherical coordinate system (see figure 11). They are considered along the polar angle θ as follows:

$$C_p(\theta) = \frac{p(\theta)}{\frac{1}{2}\rho U_\infty^2} \tag{22}$$

The pressure coefficient distribution according to θ is compared for $Re = 1, 10, 100$ to some available body fitted simulations results conducted by Magnaudet [47], Dennis & Walker [46], LeClair & al. [48] and Massol [23]. The

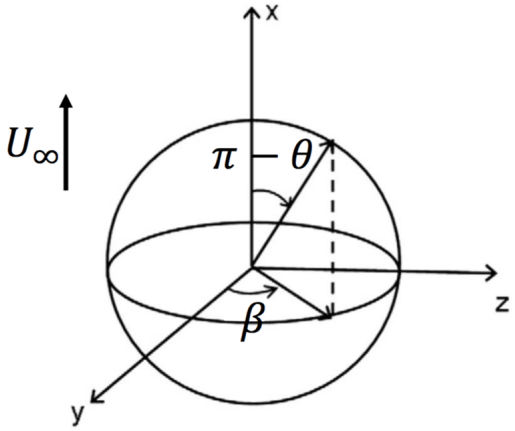

Fig. 11: Spherical coordinate system around a particle. The flow direction is represented by the undisturbed velocity U_∞.

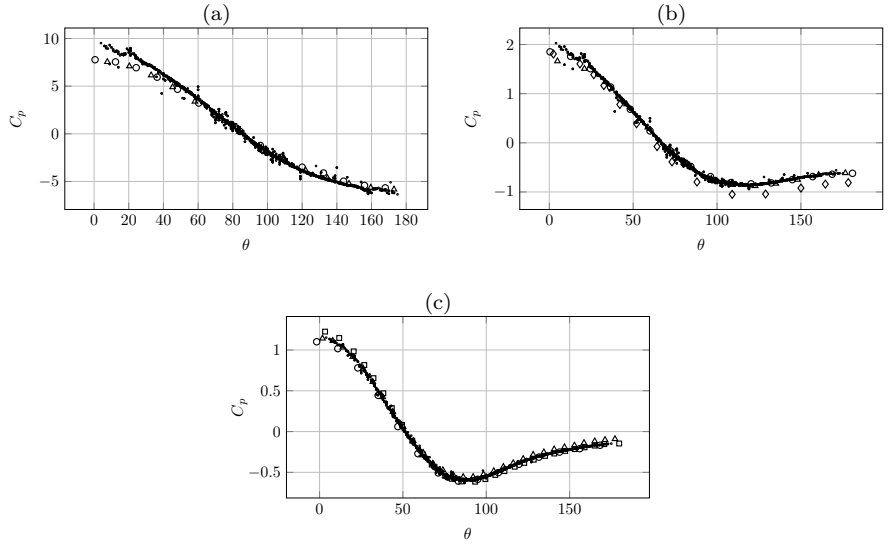

Fig. 12: Pressure coefficient for a uniform flow past an isolated sphere at $(a)Re = 1$, $(b)Re = 10$,$(c)Re = 100$: ($\diamond$) Dennis & al. [46], ($\triangle$) Magnaudet & al.[47], ($\bigcirc$) LeClair & al. [48], ($\square$) Massol [23], and ($\bullet$) present work

results are presented in figure 12. It can be observed that a very good agreement is found between our force calculations and reference results. We can observe that the local pressure profile is symmetric with respect to $\theta = 90$ for $Re = 1$ as shown in figure 12 a) and become increasingly asymmetric while increasing the Reynolds number in figures 12 b) and c). This feature of the flow is clearly highlighted for $Re = 10$ where the local pressure profile is no more symmetric with a negative pressure region that took place after $\theta = 60$. For $Re = 100$, the same conclusion holds where the negative pressure region appears at $\theta = 50$.

5 Forces in fixed arrangements of spheres

In the previous section, we have exhibited various successfull validations of the force calculation for uniform flows past a fixed isolated sphere. We can now confidently complexify the simulated particulate motion by investigating a flow past fixed particle assemblies which corresponds to a gas-solid flow with high Stokes number. Two way are possible to set up a uniform flow past fixed packed particles:

- by imposing a constant pressure gradient in the domain. In this configuration, the mean fluid velocity $\langle \mathbf{u}_f \rangle = \dfrac{\int_V (1-C)\mathbf{u}dV}{\int_V (1-C)dV}$ evolves to reach a steady state corresponding to the imposed pressure gradient.
- by choosing a desired mean fluid velocity $\langle \mathbf{u}_f \rangle = \mathbf{u}_d$, and so a desired Reynolds number. A source term $\mathbf{F}_m = -\rho \dfrac{\langle \mathbf{u}_f \rangle - \mathbf{u}_d}{\Delta t} + \dfrac{\sum_i^{N_p} \mathbf{F}_i^D}{V_f}$ is inserted in the momentum conservation equations. It is adjusted until the desired Reynolds number is reached. This is the method used in this work. Its main advantage is to be able to simulate a prescribed Reynolds number without a trial and error procedure unlike to what is require in the pressure gradient technique.

Two ways to distribute the particles are studied in this work: a Face-Centered Cubic arrangement of spheres for both mono and bi-dispersed flows, and random assemblies of spheres only for mono-dispersed flows.

The particulate Reynolds number $Re = \dfrac{|\langle \mathbf{u}_f \rangle| d}{\nu}$ is used studying the Face-Centered Cubic arrangement of spheres following the work of Massol [23]. On the other hand, in the random assemblies of spheres, another Reynolds number based on the superficial velocity $(1-\alpha_d)|\langle \mathbf{u}_f \rangle|$ is considered to take into account the solid loading in the characterization of the flows [22][19]. It is given by:

$$Re_S = \frac{(1-\alpha_d)|\langle \mathbf{u}_f \rangle| d}{\nu} \tag{23}$$

The relation between the solid volume fraction α_d and the number of particle N_p is:

$$N_p = \frac{6}{\pi}\left(\frac{L}{D}\right)^3 \alpha_d \tag{24}$$

As for the uniform flow past an isolated sphere, the grid resolution is fixed by imposing 5 Cartesian cells in the boundary layer as $\Delta x = \dfrac{d}{5\sqrt{Re_S}}$.

The mean non-dimensional drag force for all the particles is then defined as:

$$F = \frac{|\langle \mathbf{F}^D \rangle|}{3\pi\mu d(1-\alpha_d)|\langle \mathbf{u}_f \rangle|} \tag{25}$$

with $\langle \mathbf{F}^D \rangle = \dfrac{1}{N_p}\sum_i^{N_p} \mathbf{F}_i^D$, $\mathbf{F}_i^D$ being the drag force computed over the i^{th} particle.

5.1 Monodispersed arrangements of spheres

5.1.1 Face-Centred Cubic periodic arrangement of spheres

A Face-Centered Cubic (FCC) array is a cube where three spheres are placed on the faces centers, and one sphere is located on the vertices with periodic boundary conditions, as illustrated in the figure 13.

This configurations was widely studied [23] [17][22] to understand and separate the wake effects, observed when spheres are aligned along the flow direction, *i.e.* streamwise interactions, from the blocking effects, where the spheres are aligned along the direction perpendicular to the flow direction, *i.e.* lateral interactions. Two regimes, *i.e.* attached and separated flows, govern the uniform flow past a FCC array of spheres, depending on the Reynolds number and the solid volume fraction. They are considered below.

Regime 1: attached flows

For low Reynolds numbers, the boundary layer remains attached to the particles. Unlike the isolated sphere configurations, the boundary layer detachment occurs for higher Reynolds numbers when FCC arrays are considered, due to the blocking effect of the surrounding particles. In fact, the presence of lateral spheres speeds-up the flow between the spheres and blocks the detachment of the boundary layer. Figure 14 illustrates this regime for $Re = 50$, $\alpha_d = 0.15$. A very good agreement is observed for the pressure distribution over the spheres in both plans $\beta = 0$ and $\beta = 45$ as shown in figure 14(a) and 14(b), compared to the results of Massol *et al.* [23] obtained with body fitted meshes. The same agreement is observed for the axial friction coefficient as illustrated in figure

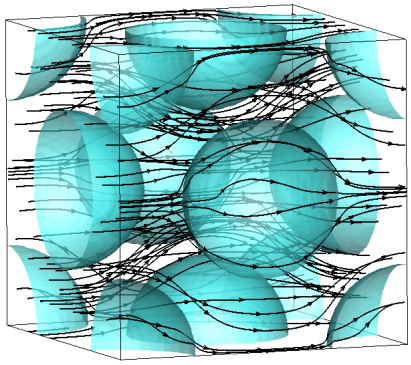

Fig. 13: Streamlines of a steady flow along the x-axis of a Face-Centred Cubic array of spheres at $Re = 50$ and $\alpha_d = 0.5$. The particle shape is plotted in blue.

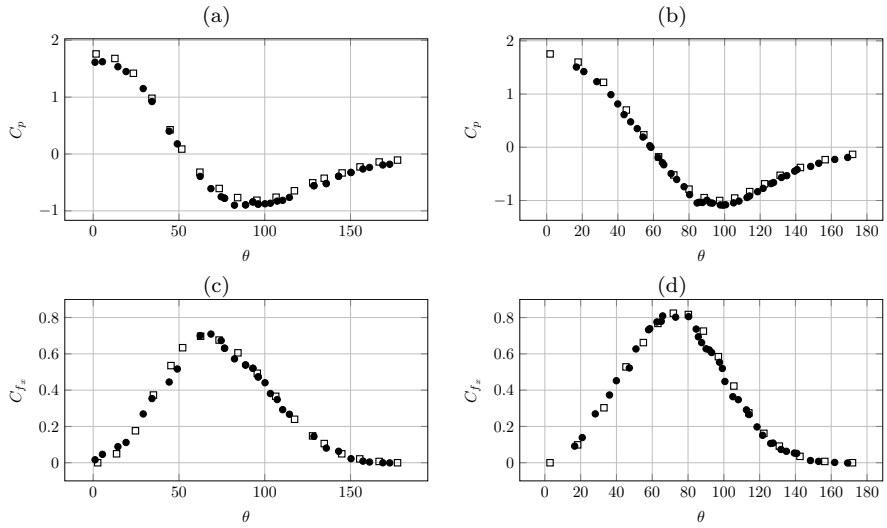

Fig. 14: Pressure coefficient $[(a)\ \beta = 0, (b)\ \beta = 45]$ and axial friction coefficient $[(c)\ \beta = 0, (d)\ \beta = 45]$, for a uniform flow past a FCC at $Re = 50, \alpha_d = 0.15$: (□) Massol *et al.* [23], and (●) present work

14(c) and 14(d) for the plans $\beta = 0$ and $\beta = 45$, the spherical coordinates α and β are illustrated in the figure 11. It is worthwhile to note that the flow is non-axisymmetric even if all particles see the same flow due to the symmetry of the array and the periodicity of boundary conditions.

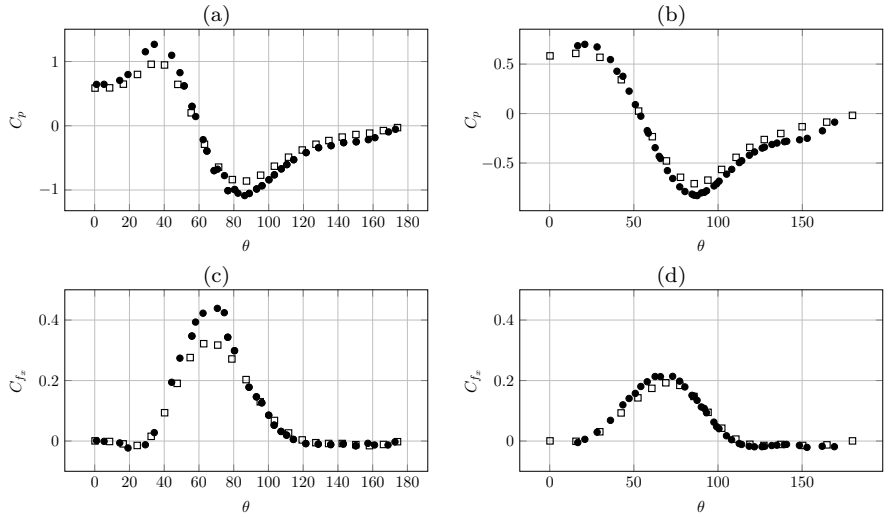

Fig. 15: Pressure coefficient [(a) $\beta = 0, (b)$ $\beta = 45$] and axial friction coefficient [(c) $\beta = 0, (d)$ $\beta = 45$], for a uniform flow past a FCC at $Re = 300, \alpha_d = 0.15$: (□) Massol *et al.* [23], and (●) present work

Regime 2: separated flows downstream of the spheres

With increasing Reynolds numbers, a separation of the boundary layer occurs in the downstream hemisphere of the particles. As noticed for an isolated sphere, the recirculating zone length increases with the Reynolds number. The flow confinement due to the presence of the lateral particles is so significant that high speed jet flows are obtained between the particles. These jet flows impact the spheres onto the upstream hemisphere. As illustrated in figure 15(a), this mechanism induces the development of a fountain effect on the vertical plan $\beta = 0$, the direct consequence of which is that the maximum pressure is no longer at $\theta = 0$ but at $\theta = 36$. Note that the same result was found by Massol *et al.* [23]. Figures 15(a) and 15(b) show again the good agreement of the pressure distribution on the vertical and lateral plans with the body fitted simulations of Massol *et al.* [23], and the same conclusions is observed in the figures 15(c) and 15(d) for the axial friction coefficient distribution. It can be noticed that for this Reynolds number of 300, larger differences are observed between our force calculation and body fitted grid results, mostly in the vicinity of the pressure peaks in the $\beta = 0$ plans.

Drag force

The drag force F normalized by the isolated sphere drag (given by Schiller [11]) $F_s = 1 + 0.15Re^{0.687}$, noted as $\dfrac{F}{F_s}$, is compared to existing literature results:

- Tenneti *et al.* [22]:

$$F_T = \frac{F_s}{(1-\alpha_d)^2} + F_\phi + F_{\phi,Re}$$

$$F_\phi = \frac{5.81\phi}{(1-\alpha_d)^2} + 0.48\frac{\alpha_d^{\frac{1}{3}}}{(1-\alpha_d)^3}$$

$$F_{\phi,Re} = (1-\alpha_d)\alpha_d^3 Re\left(0.95 + \frac{0.61\alpha_d^3}{(1-\alpha_d)^2}\right)$$

- Gobin *et al.* [14]:

$$F_G = \begin{cases} F_{WY} & \text{if} \quad \alpha_d \leq 0.3 \\ \min(F_{WY}, F_E) & \text{otherwise} \end{cases}$$

$$F_{WY} = F_s(1-\alpha_d)^{-3.7} \qquad \text{Wen\&Yu[13]}$$

$$F_E = \frac{150}{18}\frac{\alpha_d}{(1-\alpha_d)^2} + \frac{7}{4}\frac{1}{18}\frac{Re}{(1-\alpha_d)^2} \quad \text{Ergun[12]}$$

- Beetstra *et al.* [19]:

$$F_B = \frac{10\alpha_d}{(1-\alpha_d)^2} + (1-\alpha_d)^2(1+1.5\sqrt{\alpha_d}) + \frac{0.413}{(1-\alpha_d)^2}\frac{Re}{24}\frac{\frac{1}{(1-\alpha_d)} + 3(1-\alpha_d)\alpha_d + 8.4Re^{-0.343}}{1+10^{3\alpha_d}Re^{-0.5-2\alpha_d}} \tag{26}$$

Comparisons with these results are presented in figure 16 at different Reynolds number $Re = 10$ figure 16(a), $Re = 50$ figure 16(b), $Re = 100$ figure 16(c) and $Re = 300$ figure 16(d). It can be observed that a nice match is found between our results and those of Massol *et al.* [23] which was extracted from body fitted simulations. Reasonable agreement is also observed with Gobin *et al.* [14], and Beetstra *et al.* [19] even if larger differences are noticed for $Re = 10$ and 300. The correlation given by Tenneti *et al.* [22] seems to differ from the other results for high solid volume fraction. Note that the works of Beetstra *et al.* [19] and Tenneti *et al.* [22] was conducted using an immersed boundary methods to carry out these simulations.

5.1.2 Random periodic arrangement of spheres

A new step is taken in the complexity of the problem by randomly distributing a set of spheres for a given solid volume fraction. An illustration is given in figure 17 for $Re_S = 50$ and $\alpha_d = 0.3$. The locations of the spheres are set by means of a classical Monte Carlo procedure to distribute them in the domain until the desired compacity is reached, and a hard sphere collisions model is used to prevent spheres from overlapping [49]. To simulate an infinite domain, periodic boundary conditions are specified in all directions.

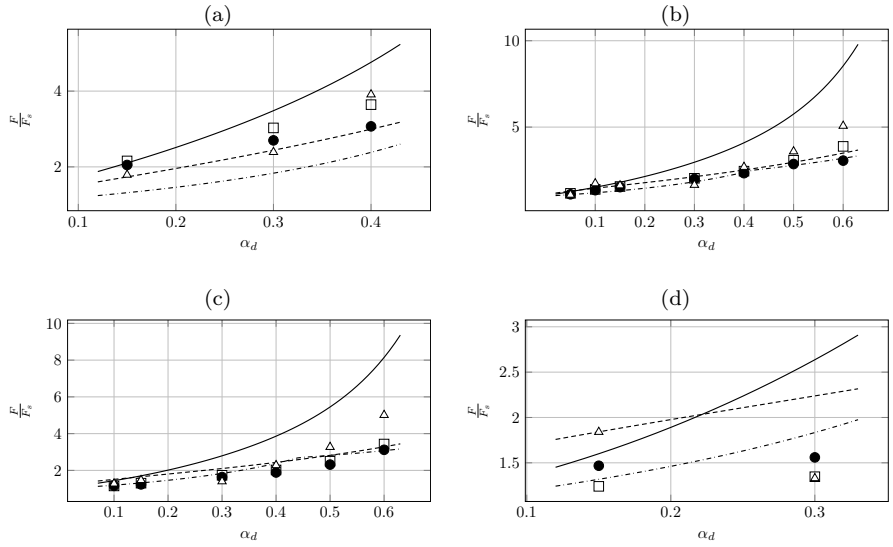

Fig. 16: Drag force for a uniform flow past a FCC, normalized by Schiller & Naumann [11] drag force for a uniform flow past an isolated sphere. Results are presented as a function of the solid volume fraction α_d and Reynolds number $(a)Re = 10$, $(b)Re = 50$,$(c)Re = 100$,$(d)Re = 300$: (——) Tenneti *et al.* [22], (-·-·) Gobin *et al.*. [14], (- - -) Beetstra *et al.* [19], (△) Randrianarivelo [24], (□) Massol *et al.* [23], and (●) present work.

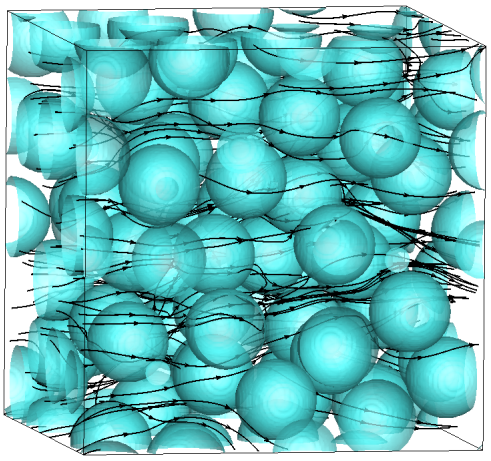

Fig. 17: Random periodic arrangement of spheres, for $Re_S = 50$ and $\alpha_d = 0.3$ - The particle shape is plotted in blue while black lines represent streamlines.

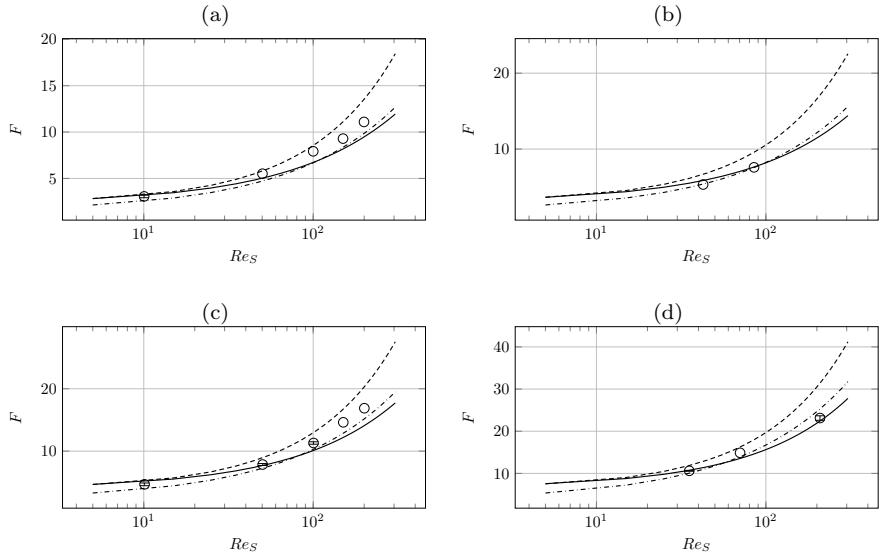

Fig. 18: Normalized drag force for a uniform flow past random packed spheres as function of the superficial Reynolds number Re_S and solid volume fraction (*a*) $\alpha_d = 0.1$, (*b*) $\alpha_d = 0.15$, (*c*) $\alpha_d = 0.2$, (*d*) $\alpha_d = 0.3$: (——) Tenneti *et al.* [22], (-·-·) Gobin *et al.* [14], (- - -) Beetstra *et al.* [19] and (○) present work. The error bars represent 95% confidence intervals in the estimation of the normalized drag force.

To be statistically converged, we performed for most cases five Multiple Independent Simulations (MIS), Tenneti *et al.* [22] conducted the same number of MIS to obtain their correlation for the drag force. Consequently, the representative non-dimensional drag force numerically obtained is an average of those calculated over the different realizations (MIS). Simulations with various solid volume fraction $\alpha_d = 0.1, 0.15, 0.2, 0.3$ have been investigated, together with different superficial Reynolds numbers ranging from 20 to 200.

The results presented in figure 18 demonstrate again a good global agreement of our results with existing correlations of Tenneti *et al.* [22], Gobin *et al.* [14] and Beetstra *et al.* [19] for each solid volume fractions studied here as shown in figures: 18(*a*) for $\alpha_d = 0.1$, 18(*b*) for $\alpha_d = 0.15$, 18(*c*) for $\alpha_d = 0.2$ and 18(*d*) for $\alpha_d = 0.3$, all function of the superficial Reynolds number. In all cases, for larger Re_S, the correlation of Beetstra *et al.* [19] is farther from other works.

The pressure profiles according to θ are given in figure 20. They have been obtained with our force calculation and our simulations. No comparisons to other works is possible as these profiles are not reported in the literature. It can be noticed that the pressure contribution on the drag force increase with

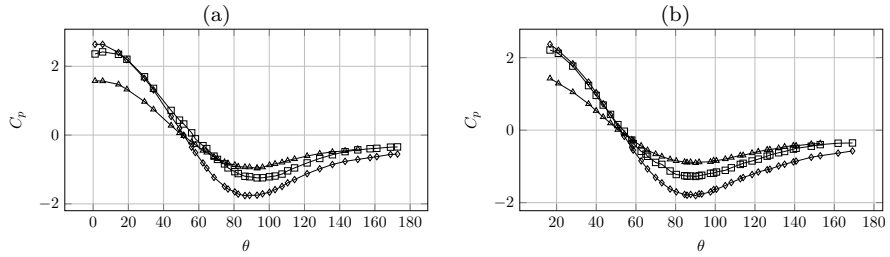

Fig. 19: Pressure coefficient for a uniform flow past random packed spheres at $Re_S = 200$ as function of α_d $(a)\beta = 0$, $(b)\beta = 45$: ($\triangle$) $\alpha_d = 0.1$, ($\square$) $\alpha_d = 0.2$ and ($\diamond$) $\alpha_d = 0.3$

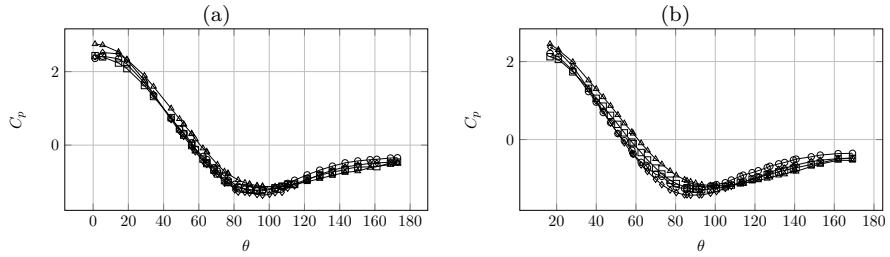

Fig. 20: Pressure coefficient for a uniform flow past random packed spheres at $\alpha_d = 0.2$ as function of Re_S $(a)\beta = 0$, $(b)\beta = 45$: ($\triangle$) $Re_S = 50$, ($\square$) $Re_S = 100$, ($\diamond$) $Re_S = 150$ and ($\bigcirc$) $Re_S = 200$

the solid volume fraction in both vertical plan $\beta = 0$ as illustrated in figure $20(a)$ and lateral plan $\beta = 45$ see figure $20(b)$. On the contrary, it seems that the Reynolds number has a small effect on the distribution of the pressure over the particles, and here again for both plans, as illustrated in figure 19. This result has previously been obtained in the study of Tenneti *et al.* [22].

As can suggest the correlation of Gobin *et al.* [14], our results (see figure 21) show that the drag force in a random arrangement of spheres is having the same dependence on the Reynolds number as for an isolated sphere. On the contrary, different behaviours are noticed for Tenneti and Beetstra simulations.

5.2 Bidisperse arrangements of spheres

For a bidisperse arrangement of sphere, *i.e.* with two types of particle size, we studied a Face-Centred Cubic periodic arrangement for the two species of spheres: the larger particles are distributed in the same configuration as the one previously presented for monodisperse arrangements while the smaller

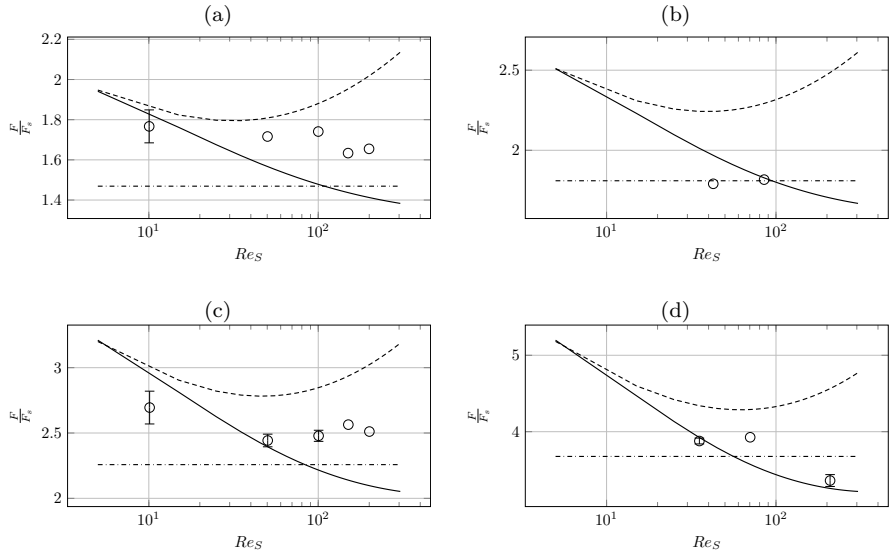

Fig. 21: Drag force for a uniform flow past random packed spheres, normalized by Schiller & Naumann [11] drag force for a uniform flow past an isolated sphere, as function of the superficial Reynolds number Re_S and solid volume fraction (*a*) $\alpha_d = 0.1$, (*b*) $\alpha_d = 0.15$, (*c*) $\alpha_d = 0.2$, (*d*) $\alpha_d = 0.3$: (——) Tenneti *et al.* [22], (-·-·-) Gobin *et al.* [14], (- - -) Beetstra *et al.* [19] and (○) present work. The error bars represent 95% confidence intervals in the estimation of the normalized drag force

particles are positioned at the center of the vertices and at the center of the cubic simulation domain. This geometry of the particle arrangement is illustrated in figure 22.

Two additional dimensionless parameters, for each species, are now necessary to characterize the flow:

$$x_i = \frac{\alpha_i}{\alpha_d} \quad , \quad y_i = \frac{d_i}{d_s} \tag{27}$$

where d_i and α_i are the particle diameter and the solid volume fraction of the specie i respectively. The Sauter mean diameter d_s is given by:

$$d_s = \left[\sum_i^2 \frac{x_i}{d_i} \right]^{-1}$$

The Sauter mean diameter is one of the most important characteristic dimension for the bidisperse particle arrangement that is often used in the literature [19].

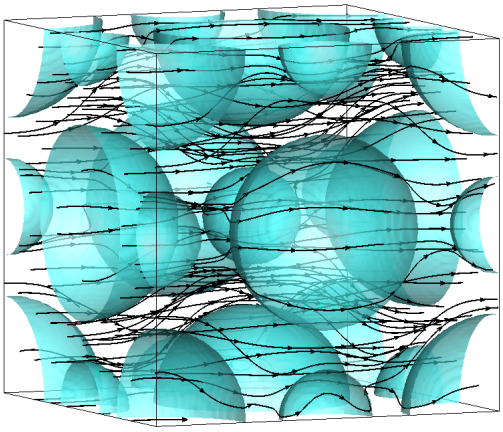

Fig. 22: FCC/FCC bidisperse arrangement of spheres for $Re = 50$ and $\alpha_d = 0.3$ - the particle shape is plotted in blue and the black lines are the streamlines.

Table 1: values of the parameters characterizing the bi-disperse flows simulated in this work.

x_1	x_2	y_1	y_2	d_s
0.88889	0.11111	1.11111	0.55556	0.0009m

We have performed simulations of FCC/FCC bidispersed arrangement of spheres, for which $\dfrac{d_1}{d_2} = 2$, at Reynolds number $Re = 50$ and 100. The solid volume fractions for the larger particles are $\alpha_1 = 0.15$ and 0.3. The corresponding values of x_i, y_i and d_s are reported in Table 1.

Our force calculation results are given in figure 23. They are compared to Beetstra *et al.* [19] correlation that provides the drag force for the i^{th} species of particle as follows:

$$(F_B)_i = ((1-\alpha_d)y_i + \alpha_d y_i^2 + 0.0064(1-\alpha_d)y_i^3)F_B$$

where F_B is the Beetstra drag force for a mono-dispersed arrangement of spheres given in equation (26). The values of forces obtained with our method are also compared to Massol body fitted results [23]. It can be observed that for all Reynolds and solid fractions, our drag forces are in better agreement with Massol simulations than with Beetstra laws extracted from their simulations. A possible explanations of the gap between Beetstra correlation and other simulations is perhaps due to the accuracy and method for calculating forces on the particles with their approach. The same kind of discrepancies have been reported for Beelstra results in random arrangements of spheres.

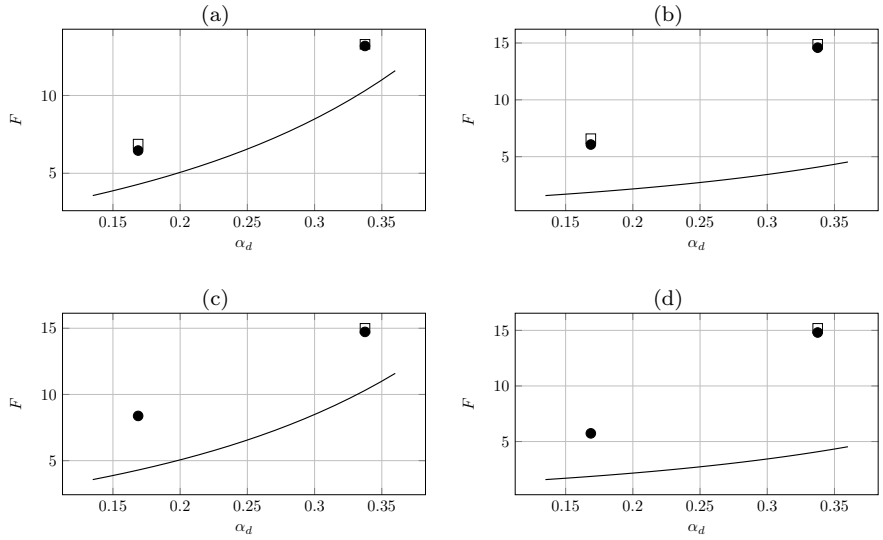

Fig. 23: Normalized drag force for a uniform flow past a FCC/FCC packed spheres as function of the solid volume fraction α_d $(a) : (Re = 50, y1)$, $(b) : (Re = 50, y2)$, $(c) : (Re = 100, y1)$, $(d) : (Re = 100, y2)$, : (——) Beetstra & al. [19] , (□) Massol [23], (●) present work.

6 Conclusions and perspectives

A new method has been designed for estimating forces in finite-size particle simulations. It is based on Lagrange extrapolation and Taylor interpolation of third order. In our method, a Lagrangian mesh is used to describe the particle shape over time on the Eulerian Cartesian mesh devoted to the flow motion. One of the most original part of our approach is to upwind the interpolation support in the normal direction to the fluid/particle interface in order to use only fluid values to estimate forces. Various parameters of the method have been tested such as effect of interpolation and extrapolation orders or the size of the particle surface elements on the error observed on forces.

Based on a second order fictitious domain method using penalty techniques and augmented Lagrangian procedures for the incompressibility constraint, we have simulated various particulate flow motions ranging from incompressible flows around an isolated particle at various Reynolds numbers to flows across packed spheres under Faced-Centered Cubic, random and bi-disperse arrangements. In all configuration, the drag forces have been compared to reference results of the literature for various solid fractions and Reynolds numbers. The general conclusion that we have obtained is that our force calculation method fits always better to body fitted simulations of Massol *et al.* [23], that can be considered as a reference, compared to other force estimates obtained with

other IBM approaches. It has also been demonstrated that having at least 5 points in the boundary layer attached to a particle ensures to recover all the physics of the interaction between the carrier fluid and particles without using any force or interaction model. To our understanding, for obtaining a correct force calculation in finite-size particle simulations, the most important parameter is not the number of Eulerian cells along a particle diameter but the number of mesh cells belonging to the boundary layer surrounding the particle, whatever the particle diameter.

Future works and ongoing developments are devoted to extending our method to heat flux calculation and extraction of heat transfer coefficients in particulate flows. Another interesting way of possible improvement of the accuracy of our approach is the use of Aslam extensions [50] to replace the Taylor interpolation in our force calculation method. Other interesting issues are the extension of the present force calculation to more complex and realistic particle shapes such as spheroid or spherocylindrical particles.

7 Acknowledgements

This work was granted access to the HPC resources of CINES under the allocation A0032b06115 made by GENCI (Grand Equipement National de Calcul Intensif), and to the resources of CALMIP supercomputing center under the allocation 2017-P1529."

Appendix 1: Taylor Interpolation

Let us consider $f : X \in \mathbb{R}^3 \rightarrow \mathbb{R}$ a n-differentiable function at a given point $\mathbf{E}$. The n^{th} order Taylor Interpolation of f at point $\mathbf{C}_l$ is:

$$f(\mathbf{C}_l) = \sum_{|\alpha|=0}^{n-1} \frac{1}{\alpha!} \frac{\partial^\alpha f}{\partial x^\alpha}(\mathbf{E})(\mathbf{C}_l - \mathbf{E})^\alpha + \mathrm{O}(||\mathbf{C}_l - \mathbf{E}||^n)$$

where $\alpha = (\alpha_1, \alpha_2, \alpha_3) \in \mathbb{N}^3$ is the sum multi-index. As described in figure 24, $\mathbf{E}$ denotes the nearest point to the Lagrangian particle surface point $\mathbf{C}_l$. Point $\mathbf{E}$ belongs to the fluid domain and so is located on the fixed Eulerian mesh.

The four first order or Taylor interpolation are the following:

- First order:

$$f(\mathbf{C}_l) = f(\mathbf{E}) + \mathrm{O}(||\mathbf{C}_l - \mathbf{E}||) \tag{28}$$

- Second order:

$$f(\mathbf{C}_l) = f(\mathbf{E}) + \frac{\partial f}{\partial x_i}(\mathbf{E})((\mathbf{C}_l)_i - \mathbf{E}_i) + \mathrm{O}(||\mathbf{C}_l - \mathbf{E}||^2) \tag{29}$$

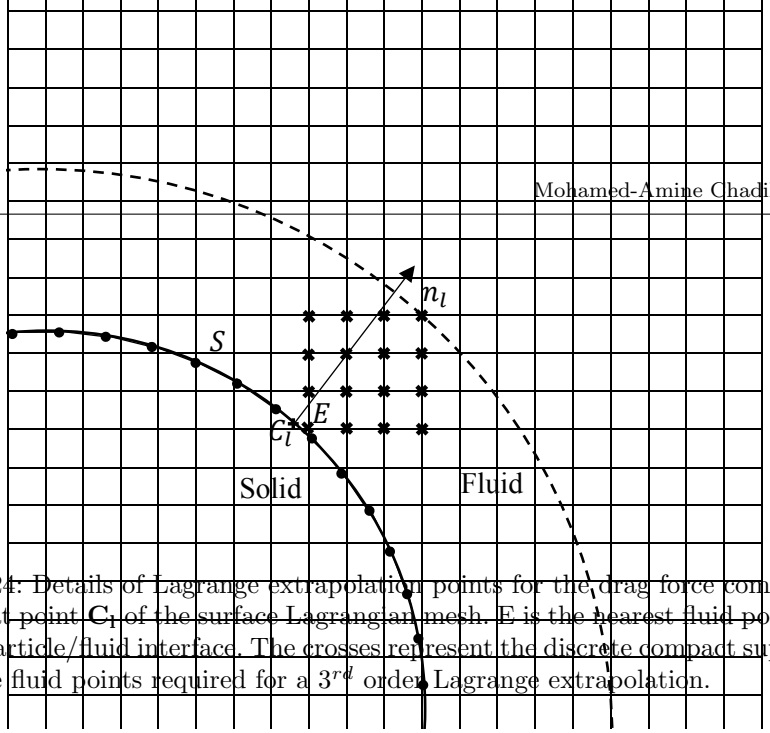

Fig. 24: Details of Lagrange extrapolation points for the drag force computation at point $\mathbf{C_l}$ of the surface Lagrangian mesh. E is the nearest fluid point to the particle/fluid interface. The crosses represent the discrete compact support of the fluid points required for a 3^{rd} order Lagrange extrapolation.

- Third order:

$$\begin{aligned} f(\mathbf{C}_l) = f(\mathbf{E}) + \frac{\partial f}{\partial x_i}(\mathbf{E})((\mathbf{C}_l)_i - \mathbf{E}_i) + \frac{1}{2}\frac{\partial^2 f}{\partial x_i^2}(\mathbf{E})((\mathbf{C}_l)_i - \mathbf{E}_i)^2 \\ + \frac{\partial^2 f}{\partial x_i \partial x_j}(\mathbf{E})((\mathbf{C}_l)_i - \mathbf{E}_i)((\mathbf{C}_l)_j - \mathbf{E}_j) + \mathrm{O}(||\mathbf{C}_l - \mathbf{E}||^3) \end{aligned} \tag{30}$$

- Fourth order:

$$\begin{aligned} f(\mathbf{C}_l) = f(\mathbf{E}) + \frac{\partial f}{\partial x_i}(\mathbf{E})((\mathbf{C}_l)_i - \mathbf{E}_i) + \frac{1}{2}\frac{\partial^2 f}{\partial x_i^2}(\mathbf{E})((\mathbf{C}_l)_i - \mathbf{E}_i)^2 \\ + \frac{\partial^2 f}{\partial x_i \partial x_j}(\mathbf{E})((\mathbf{C}_l)_i - \mathbf{E}_i)((\mathbf{C}_l)_j - \mathbf{E}_j) + \frac{1}{6}\frac{\partial^3 f}{\partial x_i^3}(\mathbf{E})((\mathbf{C}_l)_i - \mathbf{E}_i)^2 \\ + \sum_{i \neq j} \frac{1}{2}\frac{\partial^3 f}{\partial x_i^2 \partial x_j}(\mathbf{E})((\mathbf{C}_l)_i - \mathbf{E}_i)^2((\mathbf{C}_l)_j - \mathbf{E}_j) \\ + \frac{\partial^3 f}{\partial x_1 \partial x_2 \partial x_3}(\mathbf{E})((\mathbf{C}_l)_1 - \mathbf{E}_1)((\mathbf{C}_l)_2 - \mathbf{E}_2)((\mathbf{C}_l)_3 - \mathbf{E}_3) \\ + \mathrm{O}(||\mathbf{C}_l - \mathbf{E}||^4) \end{aligned} \tag{31}$$

For each order of interpolation, we have to discretize the partial derivative used in it by considering the same order of discretization. To avoid using solid point in the approximation of these derivatives, we choose to use, depending on the sign of the outgoing normal vector $\mathbf{n}_l$, a forward (resp. a backward) difference scheme if $(\mathbf{n}_l)_i > 0$ (resp. $(\mathbf{n}_l)_i < 0$). The forward difference scheme for the derivatives used in (28), (29), (30), (31) is detailed below. The backward difference scheme is straightforwardly obtained.

Gradient approximation

$$\frac{\partial f}{\partial x_i} = \frac{3f_i - 4f_{i+1} + f_{i+2}}{-2\Delta x_i} + \mathrm{O}(||\Delta x||^2)$$

$$\frac{\partial f}{\partial x_i} = \frac{11f_i - 18f_{i+1} + 9f_{i+2} - 2f_{i+3}}{-6\Delta x_i} + \mathrm{O}(||\Delta x||^3)$$

$$\frac{\partial f}{\partial x_i} = \frac{25f_i - 48f_{i+1} + 36f_{i+2} - 16f_{i+3} + 3f_{i+4}}{-12\Delta x_i} + \mathrm{O}(||\Delta x||^4)$$

Hessian approximation

$$\frac{\partial^2 f}{\partial x_i^2} = \frac{35f_i - 104f_{i+1} + 114f_{i+2} - 56f_{i+3} + 11f_{i+4}}{12\Delta x_i^2} + \mathrm{O}(||\Delta x||^3)$$

$$\begin{aligned}\frac{\partial^2 f}{\partial x_i \partial x_j} = &\frac{539f_{i,j} - 781f_{i+1,j} + 297f_{i+2,j} - 55f_{i+3,j} - 781f_{i,j+1} + 1035f_{i+1,j+1}}{192\Delta x_i \Delta x_j} \\ &\frac{-303f_{i+2,j+1} + 49f_{i+3,j+1} + 297f_{i,j+2} - 303f_{i+1,j+2} + 3f_{i+2,j+2}}{192\Delta x_i \Delta x_j} \\ &+ \frac{3f_{i+3,j+2} - 55f_{i,j+3} + 49f_{i+1,j+3} + 3f_{i+2,j+3} + 3f_{i+3,j+3}}{192\Delta x_i \Delta x_j} \\ &+ \mathrm{O}(||\Delta x||^3)\end{aligned}$$

$$\frac{\partial^2 f}{\partial x_i^2} = \frac{45f_i - 154f_{i+1} + 214f_{i+2} - 156f_{i+3} + 61f_{i+4} - 10f_{i+5}}{12\Delta x_i^2} + \mathrm{O}(||\Delta x||^4)$$

$$\begin{aligned}\frac{\partial^2 f}{\partial x_i \partial x_j} = &\frac{117f_{i,j} - 73f_{i+1,j} - 83f_{i+2,j} + 42f_{i+3,j} - 3f_{i+4,j} - 73f_{i,j+1} - 243f_{i+1,j+1}}{60\Delta x_i \Delta x_j} \\ &\frac{477f_{i+2,j+1} - 173f_{i+3,j+1} + 12f_{i+4,j+1} - 83f_{i,j+2} + 477f_{i+1,j+2}}{60\Delta x_i \Delta x_j} \\ &+ \frac{-528f_{i+2,j+2} + 137f_{i+3,j+2} - 3f_{i+4,j+2} + 42f_{i,j+3} - 173f_{i+1,j+3}}{60\Delta x_i \Delta x_j} \\ &+ \frac{137f_{i+2,j+3} - 3f_{i+3,j+3} - 3f_{i+4,j+3} - 3f_{i,j+4} + 12f_{i+1,j+4} - 3f_{i+2,j+4}}{60\Delta x_i \Delta x_j} \\ &+ \frac{-3f_{i+3,j+4} - 3f_{i+4,j+4}}{60\Delta x_i \Delta x_j} + \mathrm{O}(||\Delta x||^4)\end{aligned}$$

Third order derivative approximation

$$\frac{\partial^3 f}{\partial x_i^3} = \frac{49f_i - 232f_{i+1} + 461f_{i+2} - 496f_{i+3} + 307f_{i+4} - 104f_{i+5} + 15f_{i+6}}{-8\Delta x_i^3} + \mathrm{O}(||\Delta x||^4)$$

$$\begin{aligned}\frac{\partial^3 f}{\partial x_i^2 \partial x_j} = & \frac{2775f_{i,j} - 8725f_{i+1,j} + 10895f_{i+2,j} - 7105f_{i+3,j} + 2550f_{i+4,j}}{-480\Delta x_i^2 \Delta x_j} \\ & \frac{-390f_{i+5,j} - 4085f_{i,j+1} + 11931f_{i+1,j+1} - 13489f_{i+2,j+1}}{-480\Delta x_i^2 \Delta x_j} \\ & + \frac{7911f_{i+3,j+1} - 2654f_{i+4,j+1} + 386f_{i+5,j+1} + 1675f_{i,j+2}}{-480\Delta x_i^2 \Delta x_j} \\ & + \frac{-3889f_{i+1,j+2} + 2856f_{i+2,j+2} - 744f_{i+3,j+2} + 101f_{i+4,j+2}}{-480\Delta x_i^2 \Delta x_j} \\ & + \frac{f_{i+5,j+2} - 385f_{i,j+3} + 711f_{i+1,j+3} - 264f_{i+2,j+3} - 64f_{i+3,j+3}}{-480\Delta x_i^2 \Delta x_j} \\ & + \frac{f_{i+4,j+3} + f_{i+5,j+3} + 10f_{i,j+4} - 14f_{i+1,j+4} + f_{i+2,j+4} + f_{i+3,j+4}}{-480\Delta x_i^2 \Delta x_j} \\ & + \frac{f_{i+4,j+4} + f_{i+5,j+4} + 10f_{i,j+5} - 14f_{i+1,j+5} + f_{i+2,j+5} + f_{i+3,j+5}}{-480\Delta x_i^2 \Delta x_j} \\ & + \frac{f_{i+4,j+5} + f_{i+5,j+5}}{-480\Delta x_i^2 \Delta x_j} + \mathrm{O}(||\Delta x||^4)\end{aligned}$$

$$
\begin{aligned}
\frac{\partial^3 f}{\partial x_1 \partial x_2 \partial x_3} = & \frac{4069 f_{i,j,k} - 13656 f_{i+1,j,k} - 6 f_{i+2,j,k} - 6 f_{i+3,j,k} - 6 f_{i+4,j,k}}{-9000 \Delta x_1 \Delta x_2 \Delta x_3} \\
& \frac{12194 f_{i,j+1,k} - 23256 f_{i+1,j+1,k} + 10194 f_{i+2,j+1,k} + 444 f_{i+3,j+1,k}}{-9000 \Delta x_1 \Delta x_2 \Delta x_3} \\
& + \frac{-306 f_{i+4,j+1,k} - 16681 f_{i,j+2,k} + 77094 f_{i+1,j+2,k} - 19206 f_{i+2,j+2,k}}{-9000 \Delta x_1 \Delta x_2 \Delta x_3} \\
& + \frac{-456 f_{i+3,j+2,k} + 294 f_{i+4,j+2,k} - 6 f_{i,j+3,k} - 52956 f_{i+1,j+3,k}}{-9000 \Delta x_1 \Delta x_2 \Delta x_3} \\
& + \frac{11244 f_{i+2,j+3,k} + 244 f_{i+3,j+3,k} - 6 f_{i+4,j+3,k} - 6 f_{i,j+4,k}}{-9000 \Delta x_1 \Delta x_2 \Delta x_3} \\
& + \frac{13794 f_{i+1,j+4,k} - 3006 f_{i+2,j+4,k} - 6 f_{i+3,j+4,k} - 6 f_{i+4,j+4,k}}{-9000 \Delta x_1 \Delta x_2 \Delta x_3} \\
& + \frac{-6 f_{i,j,k+1} + 18294 f_{i+1,j,k+1} + 744 f_{i+2,j,k+1} - 6 f_{i+3,j,k+1}}{-9000 \Delta x_1 \Delta x_2 \Delta x_3} \\
& + \frac{-6 f_{i+4,j,k+1} + 59869 f_{i,j+1,k+1} - 6 f_{i+1,j+1,k+1} - 6 f_{i+2,j+1,k+1}}{-9000 \Delta x_1 \Delta x_2 \Delta x_3} \\
& + \frac{-6 f_{i+3,j+1,k+1} - 6 f_{i+4,j+1,k+1} - 177281 f_{i,j+2,k+1} - 40506 f_{i+1,j+2,k+1}}{-9000 \Delta x_1 \Delta x_2 \Delta x_3} \\
& + \frac{-756 f_{i+2,j+2,k+1} - 6 f_{i+3,j+2,k+1} - 6 f_{i+4,j+2,k+1} + 153019 f_{i,j+3,k+1}}{-9000 \Delta x_1 \Delta x_2 \Delta x_3} \\
& + \frac{26994 f_{i+1,j+3,k+1} + 1494 f_{i+2,j+3,k+1} - 6 f_{i+3,j+3,k+1} - 6 f_{i+4,j+3,k+1}}{-9000 \Delta x_1 \Delta x_2 \Delta x_3} \\
& + \frac{-34281 f_{i,j+4,k+1} - 7506 f_{i+1,j+4,k+1} - 6 f_{i+2,j+4,k+1} - 6 f_{i+3,j+4,k+1}}{-9000 \Delta x_1 \Delta x_2 \Delta x_3} \\
& + \frac{-6 f_{i+4,j+4,k+1} - 7581 f_{i,j,k+2} + 3444 f_{i+1,j,k+2} - 4356 f_{i+2,j,k+2}}{-9000 \Delta x_1 \Delta x_2 \Delta x_3} \\
& + \frac{-606 f_{i+3,j,k+2} + 144 f_{i+4,j,k+2} - 136281 f_{i,j+1,k+2}}{-9000 \Delta x_1 \Delta x_2 \Delta x_3} \\
& + \frac{-4506 f_{i+1,j+1,k+2} + 3744 f_{i+2,j+1,k+2} - 6 f_{i+3,j+1,k+2} - 6 f_{i+4,j+1,k+2}}{-9000 \Delta x_1 \Delta x_2 \Delta x_3} \\
& + \frac{348519 f_{i,j+2,k+2} + 3744 f_{i+1,j+2,k+2} - 6 f_{i+2,j+2,k+2} - 6 f_{i+3,j+2,k+2}}{-9000 \Delta x_1 \Delta x_2 \Delta x_3} \\
& + \frac{-6 f_{i+4,j+2,k+2} - 257481 f_{i,j+3,k+2} - 6 f_{i+1,j+3,k+2} - 6 f_{i+2,j+3,k+2}}{-9000 \Delta x_1 \Delta x_2 \Delta x_3} \\
& + \frac{-6 f_{i+3,j+3,k+2} - 6 f_{i+4,j+3,k+2} + 51294 f_{i,j+4,k+2} - 6 f_{i+1,j+4,k+2}}{-9000 \Delta x_1 \Delta x_2 \Delta x_3} \\
& + \frac{-6 f_{i+2,j+4,k+2} - 6 f_{i+3,j+4,k+2} - 6 f_{i+4,j+4,k+2} - 6 f_{i,j,k+3}}{-9000 \Delta x_1 \Delta x_2 \Delta x_3} \\
& + \frac{-1206 f_{i+1,j,k+3} - 6 f_{i+2,j,k+3} + 494 f_{i+3,j,k+3} - 6 f_{i+4,j,k+3}}{-9000 \Delta x_1 \Delta x_2 \Delta x_3} \\
& + \frac{97519 f_{i,j+1,k+3} - 6 f_{i+1,j+1,k+3} - 6 f_{i+2,j+1,k+3} - 6 f_{i+3,j+1,k+3}}{-9000 \Delta x_1 \Delta x_2 \Delta x_3} \\
& + \frac{-6 f_{i+4,j+1,k+3} - 212981 f_{i,j+2,k+3} - 6 f_{i+1,j+2,k+3} - 6 f_{i+2,j+2,k+3}}{-9000 \Delta x_1 \Delta x_2 \Delta x_3} \\
& + \frac{-6 f_{i+3,j+2,k+3} - 6 f_{i+4,j+2,k+3} + 136469 f_{i,j+3,k+3} - 6 f_{i+1,j+3,k+3}}{-9000 \Delta x_1 \Delta x_2 \Delta x_3} \\
& + \frac{-6 f_{i+2,j+3,k+3} - 6 f_{i+3,j+3,k+3} - 6 f_{i+4,j+3,k+3} - 20181 f_{i,j+4,k+3}}{-9000 \Delta x_1 \Delta x_2 \Delta x_3}
\end{aligned}
$$

$$
\begin{aligned}
&+ \frac{-6f_{i+1,j+4,k+3} - 6f_{i+2,j+4,k+3} - 6f_{i+3,j+4,k+3} - 6f_{i+4,j+4,k+3}}{-9000\Delta x_1 \Delta x_2 \Delta x_3} \\
&+ \frac{-6f_{i,j,k+3} + 294f_{i+1,j,k+3} - 6f_{i+2,j,k+3} - 6f_{i+3,j,k+3} - 6f_{i+4,j,k+3}}{-9000\Delta x_1 \Delta x_2 \Delta x_3} \\
&+ \frac{-19531f_{i,j+1,k+3} - 6f_{i+1,j+1,k+3} - 6f_{i+2,j+1,k+3} - 6f_{i+3,j+1,k+3}}{-9000\Delta x_1 \Delta x_2 \Delta x_3} \\
&+ \frac{-6f_{i+4,j+1,k+3} + 38294f_{i,j+2,k+3} - 6f_{i+1,j+2,k+3} - 6f_{i+2,j+2,k+3}}{-9000\Delta x_1 \Delta x_2 \Delta x_3} \\
&+ \frac{-6f_{i+3,j+2,k+3} - 6f_{i+4,j+2,k+3} - 18931f_{i,j+3,k+3} - 6f_{i+1,j+3,k+3}}{-9000\Delta x_1 \Delta x_2 \Delta x_3} \\
&+ \frac{-6f_{i+2,j+3,k+3} - 6f_{i+3,j+3,k+3} - 6f_{i+4,j+3,k+3} - 6f_{i,j+4,k+3}}{-9000\Delta x_1 \Delta x_2 \Delta x_3} \\
&+ \frac{-6f_{i+1,j+4,k+3} - 6f_{i+2,j+4,k+3} - 6f_{i+3,j+4,k+3} - 6f_{i+4,j+4,k+3}}{-9000\Delta x_1 \Delta x_2 \Delta x_3} \\
&+ \mathrm{O}(||\Delta x||^4)
\end{aligned}
$$

References

1. H. H. Hu, D. D. Joseph, and M. J. Crochet. Direct Simulation of Fluid Particle Motions. *Theoretical and Computational Fluid Mechanics*, 3:285–306, 1992.
2. H. H. Hu, N. A. Patankar, and M. Y. Zhu. Direct Numerical Simulations of Fluid-Solid Systems Using the Arbitrary Lagrangian-Eulerian Technique. *Journal of Computational Physics*, 169:427–462, 2001.
3. B. Maury. Direct simulations of 2D fluid-particle flows in biperiodic domains. *Journal of Computational Physics*, 156:325–351, 1999.
4. S.H. Cho, H.G. Choi, and J.Y. Yoo. Direct numerical simulation of fluid flow laden with many particles. *International Journal of Multiphase Flow*, 31:435–451, 2005.
5. C. Dobrzynski and P. Frey. Anisotropic Delaunay Mesh Adaptation for Unsteady Simulations . In *Proceedings of the* 17^{th} *International Meshing Roundtable*, 2008.
6. R. Glowinski T. W. Pan, T. I. Hesla, D.D. Joseph, and J. Périaux. A fictitious domain approach to the direct numerical simulation of incompressible viscous flow past moving rigid bodies: application to particulate flow. *Journal of Computational Physics*, 169:363–426, 2001.
7. K. Khadra, Ph. Angot, S. Parneix, and J.P. Caltagirone. Fictitious domain approach for numerical modelling of Navier-Stokes equations. *International Journal for Numerical Methods in Fluids*, 34:651–684, 2000.
8. S. Vincent, J.-P. Caltagirone, P. Lubin, and N. Randrianarivelo. An adaptative augmented Lagrangian method for three-dimensional multi-material flows. *Computers and Fluids*, 33:1273–1289, 2004.
9. S. Vincent, T. Randrianarivelo, G. Pianet, and J.P. Caltagirone. Local penalty methods for flows interacting with moving solids at high Reynolds numbers. *Computers and Fluids*, 36:902–913, 2007.
10. S. Vincent, J. C. Brändle de Motta, A. Sarthou, J.-L. Estivalezes, O. Simonin, and E. Climent. A Lagrangian VOF tensorial penalty method for the DNS of resolved particle-laden flows. *Journal of Compuataional Physics*, 256:582–614, 2014.
11. L. Schiller and A. Z. Naumann. Über die grundlegenden Berechnungen bei der Schwerkraftaufbereitung. *Ver. Deut. Ing.*, 77:318–320, 1933.
12. Sabri Ergun. Fluid flow through packed columns. *Chemical Engineering Progress*, (48):89–94, 1952.

13. C.-Y. Wen and Y. H. Yu. Mechanics of fluidization. *Chemical Engineering Progress Symposium Series*, (62):100–111, 1966.
14. Anne Gobin, Hervé Neau, Olivier Simonin, Jean-Richard Llinas, Vince Reiling, and Jean-Lofc Sélo. Fluid dynamic numerical simulation of a gas phase polymerization reactor. *International Journal for Numerical Methods in Fluids*, 43(10-11):1199–1220, 2003.
15. Anthony J. C. Ladd. Numerical simulations of particulate suspensions via a discretized Boltzmann equation. Part 1. Theoretical foundation. *Journal of Fluid Mechanics*, 271:285, July 1994.
16. Anthony J. C. Ladd. Numerical simulations of particulate suspensions via a discretized Boltzmann equation. Part 2. Numerical results. *Journal of Fluid Mechanics*, 271:311, July 1994.
17. Reghan J. Hill, Donald L. Koch, and Anthony J. C. Ladd. Moderate-Reynolds-number flows in ordered and random arrays of spheres. *Journal of Fluid Mechanics*, 448, December 2001.
18. M. A. Van Der Hoef, R. Beetstra, and J. A. M. Kuipers. Lattice-Boltzmann simulations of low-Reynolds-number flow past mono- and bidisperse arrays of spheres: results for the permeability and drag force. *Journal of Fluid Mechanics*, 528, April 2005.
19. R. Beetstra, M. A. van der Hoef, and J. A. M. Kuipers. Drag force of intermediate Reynolds number flow past mono- and bidisperse arrays of spheres. *AIChE Journal*, 53(2):489–501, February 2007.
20. M. Uhlmann. An immersed boundary method with direct forcing for the simulation of particulate flows. *Journal of Computational Physics*, 209(2):448–476, 2005.
21. M. Uhlmann. Interface-resolved direct numerical simulation of vertical particulate channel flow in the turbulent regime. *Physics of Fluids*, 20(5):053305, 2008.
22. S. Tenneti, R. Garg, and S. Subramaniam. Drag law for monodisperse gas-solid systems using particle-resolved direct numerical simulation of flow past fixed assemblies of spheres. *International Journal of Multiphase Flow*, 37(9):1072–1092, November 2011.
23. Alexandre Massol. *Simulations numériques d'écoulements travers des réseaux fixes de spheres monodisperses et bidisperses, pour des nombres de Reynolds modérés*. PhD thesis, 2004.
24. Tseheno Nirina Randrianarivelo. *Etude numérique des interactions hydrodynamiques fluides/solides : application aux lits fluidisés*. PhD thesis, Université Bordeaux 1, 2005.
25. W. P. Breugem. A second-order accurate immersed boundary method for fully resolved simulations of particle-laden flows. *Journal of Computational Physics*, 231:4469–4498, 2012.
26. W. Bizid, A. Etcheverlepo, S. Vincent, J.-P. Caltagironeand, D. MONFORT, and M. Hassine. Penalty methods for turbulent flows interacting with obstacles. *Notes On Numerical Fluid Mech. And Multidisciplinary Design*, 125:13–22, 2014.
27. H. Ali and S. Rohani. Dynamic modeling and simulation of a risertype fluid catalytic cracking unit. *Chemical Engineering and Science*, 20:118–130, 1997.
28. Y. Zhang, Z. Chao, and H. A. Jakobsen. Modelling and simulation of chemical looping combustion process in a double loop circulating fluidized bed reactor. *Chemical Engineering Journal*, 320:271–282, 2017.
29. A. Ozel, J.C. Brändle de Motta, M. Abbas, P. Fède, O. Masbernat, S. Vincent, J.-L. Estivalezes, and O. Simonin. Particle resolved direct numerical simulation of a liquidsolid fluidized bed: Comparison with experimental data. *International Journal of Multiphase Flow*, 89:228–240, 2017.
30. T. N. Randrianarivelo, S. Vincent, O. Simonin, and J.-P. Caltagirone. A DNS approach dedicated to the analysis of fluidized beds. *Fluid Mechanics Applications*, 81:207–214, 2007.
31. Wided Bizid. *Development of penalty methods for the simulation of turbulent flows around obstacles*. PhD thesis, Bordeaux University, 2017.
32. M. Zastawny, G. Mallouppas, F. Zhao, and B. van Wachem. Derivation of drag and lift force and torque coefficients for non-spherical particles in flows. *International journal of Multiphase Flow*, (39):227–239, 2012.
33. A. Sarthou, S. Vincent, and J.-P. Caltagirone. A second-order curvilinear to cartesian transformation of immersed interfaces and boundaries. application to fictitious domains and multiphase flows. *Computers and Fluids*, 46:422–428, 2014.

34. T.N. Randrianarivelo, G. Pianet, S. Vincent, and J.-P. Caltagirone. Numerical modelling of the solid particle motion using a new penalty method. *International Journal for Numerical Methods in Fluids*, 47:1245–1251, 2005.
35. I. Kataoka. Local instant formulation of two-phase flow. *International Journal of Multiphase Flow*, 12:745–758, 1986.
36. J. C. Brändle De Motta, S. Vincent, J.-L. Estivalezes, and E. Climent. Fictitious Domain Methods and Penalty Techniques for the Simulation of Turbulent Particulate Flows. *ASME Fluid Summer Meeting, Montreal, August 4-7*, 2010.
37. W.-P. Breugem. A Combined Soft-Sphere Collision for Immersed Boundary Method for Resolved Simulations of Particulate Flows. In *Proceedings of the ASME 2010 3rd Joint US-European Fluids Engineering Summer Meeting and*, Montréal, 2010.
38. David Eberly. Quaternion algebra and calculus. Technical report, 1999.
39. J.-P. Caltagirone and S. Vincent. Tensorial penalisation method for solving Navier–Stokes equations. *Comptes Rendus de l'Académie des Sciences Paris, Série IIb*, 329:607–613, 2001.
40. M. Fortin and R. Glowinski. *Méthodes de lagrangien augmenté. Application à la résolution numérique de problèmes aux limites*. Dunod, Paris, 1982.
41. S. Vincent, A. Sarthou, J.-P. Caltagirone, F. Sonilhac, P. Février, C. Mignot, and G. Pianet. Augmented Lagrangian and penalty methods for the simulation of two-phase flows interacting with moving solids. Application to hydroplaning flows interacting with real tire tread patterns. *Journal of Computational Physics*, 230:956–983, 2011.
42. I. Gustafsson. *On first- and second-order symmetric factorisation methods for the solution of elliptic difference equations*. Chalmers University of Technology, 1978.
43. H. Van der Vost. Bi-CGSTAB: a fast and smoothly converging variant of Bi-CG for the solution of non-symmetric systems. *SIAM Journal of Scientific Computing*, 33:631–644, 1992.
44. George Keith Batchelor. *An introduction to fluid dynamics*. Cambridge mathematical library. Cambridge Univ. Press, Cambridge, 1. cambridge mathematical ed., 14. print edition, 1967. OCLC: 838184093.
45. R. Clift, J.R. Grace, and M.E. Weber. *Bubbles, Drops, and Particles*. Academic Press, 1978.
46. S. C. R. Dennis and J. D. A. Walker. Calculation of the steady flow past a sphere at low and moderate reynolds numbers. *Journal of Fluid Mechanics*, 48(4):771789, 1971.
47. Jacques Magnaudet, Mayela Rivero, and Jean Fabre. Accelerated flows past a rigid sphere or a spherical bubble. Part 1. Steady straining flow. *Journal of Fluid Mechanics*, 284(-1):97, February 1995.
48. B. P. Le Clair, A. E. Hamielec, and H. R. Pruppacher. A numerical study of the drag on a sphere at low and intermediate reynolds numbers. *Journal of the Atmospheric Sciences*, 27(2):308–315, 1970.
49. Charles S. Campbell and Christopher E. Brennen. Computer simulation of granular shear flows. *Journal of Fluid Mechanics*, 151:167188, 1985.
50. T. Aslam. A partial differential equation approach to multidimensional extrapolation. *Journal of Computational Physics*, (193):349–355, 2004.